Hoang Thai Nguyen
Theoretical and Applied Mechanics Program and Department of Civil & Environmental Engineering,
Northwestern University,
Evanston, IL 60208
e-mail: hoangnguyen2015@u.northwestern.edu

Madura Pathirage
Department of Civil & Environmental Engineering,
Northwestern University,
Evanston, IL 60208
e-mail: madurapathirage2014@u.northwestern.edu

Gianluca Cusatis
Professor of Civil and Environmental Engineering,
Department of Civil & Environmental Engineering,
Northwestern University,
Evanston, IL 60208
e-mail: g-cusatis@northwestern.edu

Zdeněk P. Bažant[1]
Walter P. Murphy Professor of Civil and Environmental Engineering,
Mechanical Engineering and Material Science and Engineering,
Department of Civil & Environmental Engineering,
Northwestern University,
Evanston, IL 60208
e-mail: z-bazant@northwestern.edu

Gap Test of Crack-Parallel Stress Effect on Quasibrittle Fracture and Its Consequences

In the standard fracture test specimens, the crack-parallel normal stress is negligible. However, its effect can be strong, as revealed by a new type of experiment, briefly named the gap test. *It consists of a simple modification of the standard three-point-bend test whose main idea is to use plastic pads with a near-perfect yield plateau to generate a constant crack-parallel compression and install the end supports with a gap that closes only when the pads yield. This way, the test beam transits from one statically determinate loading configuration to another, making evaluation unambiguous. For concrete, the gap test showed that moderate crack-parallel compressive stress can increase up to 1.8 times the Mode I (opening) fracture energy of concrete, and reduce it to almost zero on approach to the compressive stress limit. To model it, the fracture process zone must be characterized tensorially. We use computer simulations with crack-band microplane model, considering both in-plane and out-of-plane crack-parallel stresses for plain and fiber-reinforced concretes, and anisotropic shale. The results have broad implications for all quasibrittle materials, including shale, fiber composites, coarse ceramics, sea ice, foams, and fone. Except for negligible crack-parallel stress, the line crack models are shown to be inapplicable. Nevertheless, as an approximation ignoring stress tensor history, the crack-parallel stress effect may be introduced parametrically, by a formula. Finally we show that the standard tensorial strength models such as Drucker–Prager cannot reproduce these effects realistically.* [DOI: 10.1115/1.4047215]

Keywords: fracture testing, fracture mechanics, fracture properties, finite element analysis, concrete, fiber-reinforced materials, computational mechanics, mixed mode fracture

1 Introduction

A simple novel experiment, named for brevity the *gap test*, was presented in Ref. [1], which showed that a moderate crack-parallel compressive stress can greatly increase the Mode-I fracture energy, G_f, of concrete, and a high stress can reduce it almost to zero. This surprising result, with its mesomechanical explanation in Ref. [1], suggests major consequences for the numerical simulations of fracture—not only for concrete but also for all quasibrittle materials. Why hasn't this phenomenon been identified before? Three reasons can be seen:

(1) All the standard notched fracture specimens (three-point-bend, compact tension, single edge-notched tension, eccentric compression, etc.) have a negligible normal stress parallel to the crack. This is nearly so even for the standard wedge-splitting specimen.
(2) Fracture analysis has generally been focused on line cracks, as in the linear elastic fracture mechanics (LEFM), originated in 1921 Griffith [2], or in the cohesive crack model (CCM), pioneered in 1959 by Barenblatt [3,4].
(3) Visually, cracks appear as lines (albeit rough), and it is obvious that a line cut in direction x in a specimen under homogeneous uniaxial stress σ_{xx} causes no stress change, which suggests that σ_{xx} should not matter for continuum models.

It is thus clear that the crack-parallel stress can matter only if the fracture process zone (FPZ) at crack front has a finite width w_c. This is known to be a property of all quasibrittle materials, which are heterogeneous materials consisting of brittle constituents and inhomogeneities not negligible compared the structure dimensions. These materials include concrete, as the archetypical case, fiber-reinforced concrete, shale and various rocks, fiber-polymer composites, coarse-grained or toughened ceramics, refractories, bone, cartilage, dentine, dental cements, biological shells, many biomaterials, stiff soils, silt, grouted soils, sea ice, consolidated snow, cold asphalt concrete, coal, various printed materials, rigid foams, wood, paper, carton, etc., and all brittle materials on the micrometer scale.

When short concrete specimens under homogeneous uniaxial compression are about to fail by axial splitting cracks [5], the fracture energy for a superposed loading in the opening mode I would clearly be zero [6–13].

This suggests that, in concrete and similar quasibrittle materials, the G_f should depend on crack-parallel stress σ_{xx} and should terminate with 0 when σ_{xx} tends to uniaxial compressive stress limit σ_c. This represents the value of crack-parallel stress that causes compressive failure in the three-point-bend specimen. Its value is slightly different from f_c (uniaxial compressive stress of 8×4 in. cylinders) due to the differences in specimen geometry and boundary conditions.

The cohesive crack model (CCM) (e.g., [14]) cannot capture the effect of crack-parallel stress σ_{xx} because it is a line crack model, in which the crack-parallel stress or strain is not the basic thermodynamic variable. It can be introduced only as a parameter, but then the dependence of G_f on the stress tensor history is missed, as documented here by an example (this is similar to the inadequacy of describing plasticity in terms of total, rather than incremental, stress-strain relations).

On the other hand, the crack-band model [14–16] (CBM), with a tensorial softening damage constitutive law, can serve this purpose, provided that the damage law used is sufficiently realistic, i.e., the constitutive damage law must capture not only tensile microcracking in the FPZ, but also the frictional slip on inclined planes (see Fig. 2 in Ref. [1]) accompanied by splitting microcracks, which dissipate more energy than the tensile microcracking and are what

[1]Corresponding author.

Contributed by the Applied Mechanics Division of ASME for publication in the Journal of Applied Mechanics. Manuscript received May 8, 2020; final manuscript received May 13, 2020; published online May 29, 2020. Assoc. Editor: Yonggang Huang.

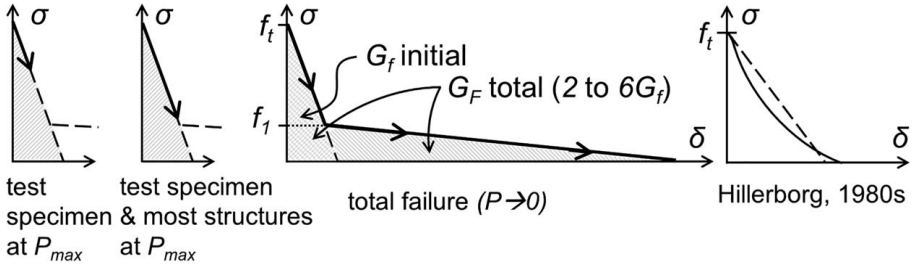

Fig. 1 Traction-separation curve without crack-parallel stress

causes the lateral expansion and longitudinal shortening of the FPZ under crack-parallel compression [17]. On the constitutive macro-level, these mechanisms cause a strong vertex effect [18–20] representing, e.g., a drastically reduced incremental stiffness for shear superposed on inelastic compression.

The microplane model for concrete used in the CBM, particularly its latest version M7 [21], has been shown to reproduce well the compression fracture as well as the measured crack-parallel stress effect on concrete [1]. M7 is adopted here to explore various interesting consequences of the new *gap test*. One feature of the microplane model that is important for the present problem is that it can reproduce the vertex effect and capture separately the frictional slip of microcracks on planes with various distinct orientations (note that the tensorially defined constitutive laws which model internal friction by interaction between the first and second invariants can make no distinction among various orientations of frictional slip). Importantly, by means of its deviatoric stress boundary, M7 automatically captures the effect of the spreading and splitting microcracks.

In discussing the fracture energy, we must first clarify what kind. The typical softening stress-separation curve of CCM of concrete begins with a steep initial tangent, followed by a very long tail, as shown in Fig. 1. This originally used curve was later found to lead to size-dependent G_F. Accordingly, two fracture energies are distinguished: (a) the initial fracture energy, G_f, given by the area under the initial tangent, and the total fracture energy, G_F, representing the area under the complete softening curve, including its tail [14,22–24]. Typically, $G_F/G_f \approx$ 2 to 6 for concretes. The G_F suffers from high uncertainty unless the work-of-fracture tests are conducted at various specimen sizes [25]. The G_f alone governs the load capacity of most structures, while the G_F governs the energy absorption in dynamic failures such as impact. Here, we consider the G_f only, from which the G_F can be inferred approximately (Fig. 1 shows also on the right softening curves without tail, which were introduced around 1980 by Hillerborg and others).

Unambiguous determination of G_f (and characteristic FPZ size c_f) from the present experiments and numerical simulations is made possible by the size effect method (see Appendix E). This method [14,26], embodied in the international standard recommendation of RILEM [27], endorsed recently by ACI-446 committee, and improved in Refs. [23,24,28], was devised in 1990 (and without c_f in 1987 [22]). It is an effective way to circumvent the impossibility of determining, optically or acoustically, the precise location of the tip of a macroscopically equivalent LEFM crack within the large FPZ of quasibrittle materials. In this method, based on asymptotic matching, it suffices to measure the maximum loads, P, of notched specimens of several sufficiently different sizes, preferably, but not necessarily, geometrically similar. The geometrically similar notched concrete beams of three sizes shown in Fig. 2 have been used here.

The preceding computer simulations [1] of the *gap test* dealt with only a few cases, with only a few levels of the crack-parallel stress, and only with concrete. These simulations demonstrated that the concrete fracture energy values measured by the *gap test* at several different crack-parallel stress levels are closely matched by the predictions of the finite element (FE) CBM with the microplane model M7 as the constitutive damage law [21,29]. Here, we continue to use the CBM with M7 to demonstrate and clarify the effect of crack-parallel stresses in many more situations. Furthermore, using the microplane model M7f [30] and the anisotropic spherocylindrical microplane model [31], we explore the crack-parallel stress effects in two other quasibrittle materials—fiber-reinforced concrete and shale.

From the practical viewpoint, this study has been motivated by the impossibility to match with the CCM the test results for shear failure of reinforced concrete beams and slabs; ditto for the splitting fracture of a sea ice plate moving against the legs of an oil platform, a vertical pavement crack under wheel load, a hydraulic crack in shale, etc.

2 Overview of Basic Aspects of the Novel Experiment—*Gap Test*

The novel, yet surprisingly simple, *gap test* [1], depicted in Fig. 3(*a*), has four key advantageous features:

(1) A pair of compressible pads (Figs. 3(*a*) and 3(*b*)) capable of nearly perfect plastic yielding (Fig. 3(*c*)) is installed next to the notch mouth to produce notch-parallel compression of desired magnitude (Fig. 3(*c*)), with no bending moment (Figs. 4(*a*)–4(*i*)).
(2) Rigid supports at beam ends are installed with a gap (of about 2–4 mm) so as to engage in contact and apply the crack-producing bending moment (Figs. 3(*a*) and 3(*b*)) only after the pads start plastic yielding (Fig. 4(*a*)-ii,iii).
(3) This way the test beam passes from one statically determinate system to another, which makes evaluation simple and unambiguous.
(4) The static determinacy of loading and the constancy of crack-parallel compression make it possible to use the size effect method, which is an easy and robust way to measure G_f, with its dependence on σ_{xx}.

The deflection relative to the end supports causes the load-deflection curve to rise above the yield plateau, peak, and then descend back to the plateau, as seen in Fig. 4(*b*). The area below this up-and-down curve is the energy dissipated by fracture, which is exploited in the work-of-fracture method of measuring fracture energy. However, only the peak loads, for several different

Fig. 2 Concrete test specimens scaled geometrically in two dimensions

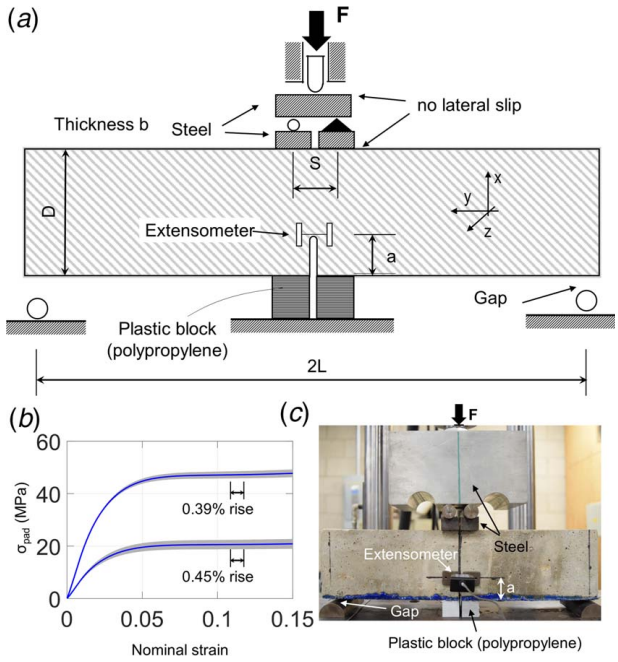

Fig. 3 (*a*) Schematic experimental setup (with coordinates *x*, *y*, *z*), (*b*) real setup, and (c) stress–strain behavior of plastic pad corresponding to two values of tested σ_{xx} (note that only a short segment of the quasi-plateau intervened during the rise of bending moment, as marked in Fig. 4(*b*)

specimen sizes, are needed to determine G_f (Fig. 4(*c*)). The typical measured curves of load P versus load-point displacement u and of P versus the crack tip opening displacement, δ_{CTOD}, are shown for $D = 101.6$ mm in Figs. 4(*b*) and 4(*c*).

The statical determinacy of the beam when the pads are yielding is gained from the constancy of the reactions of the pads. It makes the pad reactions equivalent to applied dead loads. Hence, after the pads begin to yield, there is again three-point bending, in which the deformation of the beam cannot break symmetry of the left and right halves of the beam, even in postpeak softening. Therefore, any small initial imperfection (such as a small Mode II component) must remain small, i.e., there is no equilibrium path bifurcation. The magnitude of the yield force is controlled by the area of the pad. Smaller yield forces are obtained by drilling holes in the pads (see Appendix D).

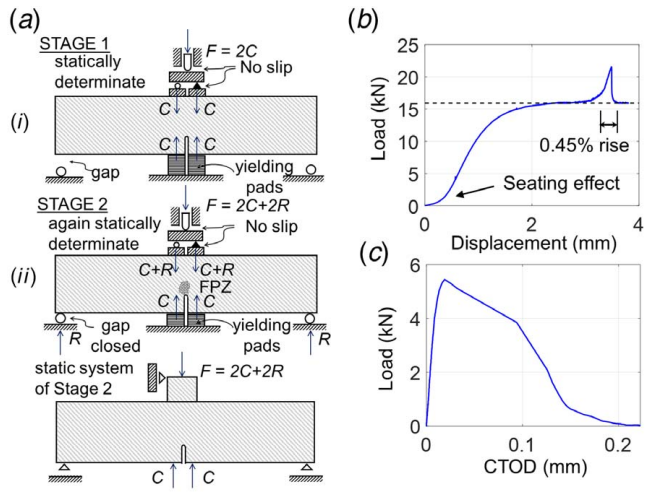

Fig. 4 (*a*) Experimental procedure, (*b*) a load-machine displacement behavior (note that within the segment *F*, which is what matters for G_f, the change in pad reaction (dashed line), is negligible, and (c) extracted load-CTOD

3 Further Aspects and Details of the Novel Experiment

The size effect method, a robust and simple method developed in 1990 [26], is what allows identifying G_f from the maximum load of fracture specimens of different sizes. Based on the Type 2 (energetic, non-statistical) size effect law of quasibrittle fracture [14,26,32–35], it has been adopted as an international standard recommendation [27] and endorsed by ACI-446 [36]. It has become the most widely used method for testing G_f of concrete and geomaterials. One advantage is that it necessitates measuring only the maximum loads, P_{max}, postpeak being superfluous, but P_{max} must be measured for at least three sufficiently different specimen sizes [26] (preferably, but not necessarily [14] scaled geometrically). As another advantage, the identification of G_f, along with the material characteristic length c_f, is reducible to linear regression. Importantly, the derivation of this method [14,26] is not affected by the crack-parallel stress, neither in-plane σ_{xx} nor anti-plane σ_{zz}.

The test specimens are analyzed as four-point-bend beams, although the two center-span loads are spaced so closely that the beams are almost equivalent to the standard three-point bend beams. To keep the evaluation simple, the separation of center-span loads was scaled with the beam size D.

Beams of three depths $D = 101.6$ mm (4 in.), 203.2 mm (8 in.), and 406.4 mm (16 in.), measured from top face to the bottom face, were tested. The span-to-depth ratio was $2L/D = 3.75$, and the notch depth ratio was $a/D = 0.3$. The beam thickness was 101.6 mm for all sizes. The beams were scaled geometrically in two dimensions (2D). Normal concrete with mean cylindrical compression strength $f_c = 40.5$ MPa was used. The maximum aggregate size was $d_a = 18$ mm. The notch width was 3 mm, which is known to be well within the admissible range compared to d_a.

The negative bending moment caused by self-weight before the pads engage is negligible (for the heaviest beam, <3% of the maximum bending moment). A small restraint against rotation ensures stability before the end supports engage [37–39].

The pads consist of a layer of polypropylene. Once plasticized, its tangential hardening shear modulus μ is very small, about 20 MPa (see Fig. 3(*c*)) (it must be nonzero, or else the plastic would escape from the pads like a fluid). During plastic compression, the polymer behaves as incompressible. The compression causes the polypropylene to be laterally squeezed out, though imperceptibly so. The lateral squeezing governs the tangential hardening stiffness H of the yielding pads, which is also very small but nonzero (see Appendix E for optimization of pad shape). The pair of elasto-plastic pads is placed next to the notch mouth (Fig. 3(*a*)), and a pair of symmetric steel loading pads on the opposite beam face. Figure 3(*c*) documents that the measured load-deflection diagram of the pads exhibits a long near-horizontal yield plateau. To lower the value of the tangential pad stiffness, H (with limited shortening of the yield plateau), regularly spaced holes are drilled through the pads (this also reduces the elastic stiffness; Fig. 3(*c*)).

To prevent shear failure of concrete under the elasto-plastic pads, a 2-mm laminate layer has been glued to the concrete surface, and it has been calculated that its effect on the stress-intensity factor is negligible. The loading rate is scaled so as to reach the maximum load within approximately the same time. An extensometer crossing the crack tip is used to measure the crack tip opening displacement δ_{CTOD} (Fig. 3(*a*) or 4(*a*)). The complete setup is seen in Fig. 4(*b*).

Each of the three data points for different σ_{xx} has been obtained by linear regression of three experiments for each of three sizes (see Fig. 5) and shown as the empty circles in Fig. 6(*a*). The coefficients of variation of the regressions (i.e., the root-mean-square of the deviations from the regression line divided by the data mean) were only 0.117, 0.135, and 0.151. These data points represent the effective values of fracture energy G_f as a function of three levels of compression stress σ_{pad} applied at the yielding pads. These experimental

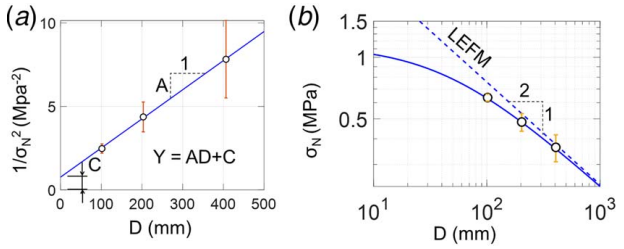

Fig. 5 (*a*) Linear regression of size effect method and (*b*) the size effect curve plotted in log-log scale

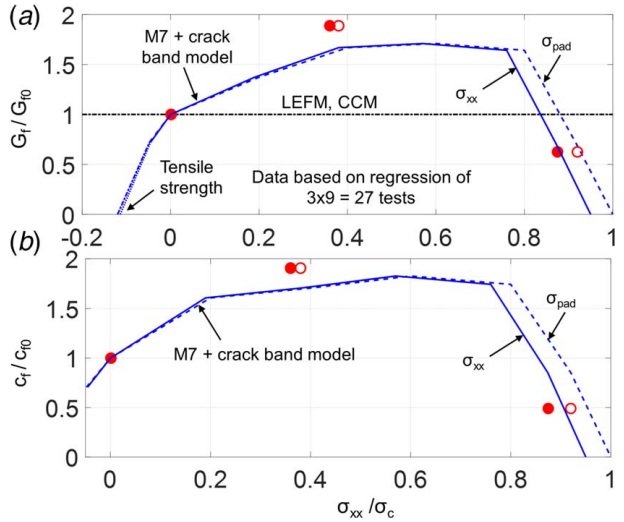

Fig. 6 (*a*) G_f (with $G_{f0} = 86.7$ N/m) as a function of σ_{pad} (dashed curve) and of σ_{xx} (solid curve) and (*b*) c_f (with $c_{f0} = 8.8$ mm) as a function of σ_{pad} (dashed curve) and of σ_{xx} (solid curve)

results [1] reveal an important fact—G_f is not constant but depends on σ_{pad}, in fact, strongly. This raises doubts about the applicability of both the LEFM and the CCM, each of which requires constancy of G_f.

To get the effective G_f as a material property, σ_{pad} must be transformed to the crack-parallel normal stress σ_{xx} at the notch tip. FE analysis was used to get the ratio $r_c = \sigma_{xx}/\sigma_{pad}$. Elastic analysis gave $r_c = 0.962$, while crack-band finite element analysis with M7 gave $r_c = 0.942$ for medium size specimens. The elastic value is seen to be a good enough approximation, with an error less than 3%. That, σ_{xx} must be less than σ_{pad} is intuitively obvious from the field of principal stress vectors obtained by FE. The data points of σ_{xx} obtained after transformation with r_c are shown as the solid circles in Fig. 6(*a*).

Alternatively, according to the classical work-of-fracture method [40–42], one could estimate the total fracture energy, G_F, via the area between the entire up-and-down curve and the horizontal yield line in Fig. 4(*c*). However, this method requires stabilizing the postpeak softening and is rather ambiguous if the correct shape of the cohesive law (Fig. 1(*a*)), is not known a priori [25]. To avoid ambiguity of G_F, the work-of-fracture test would have to be also conducted for several sufficiently different specimen sizes [25].

4 Physical Mechanism of Crack-Parallel Stress Effect on G_f

The mechanism was briefly discussed in Ref. [1] and here we are more specific. Depending on the magnitude of crack parallel compressive stress σ_{xx} (negative for compression), we can distinguish two different regimes of FPZ behavior, explained by two different mesoscale mechanisms:

Regime 1: Friction: Moderate σ_{xx} increases static friction which prevents slip and provides confinement without damage. This tends to increase strength and may be explained by the increase of interlocking and increase of static friction on rough inclined surfaces. For $\sigma_{xx} = 0$, the deviatoric (or shear) stress intensity $\tau = \tau_a$, shown in the figure, corresponds to hydrostatic pressure $p = p_a = -\sigma_{yy}/3$, where σ_{yy} is the tensile normal stress caused by beam bending in the FPZ at crack or notch front (see Fig. 7(*a*); $\tau = \sqrt{J_2}$ where $J_2 =$ second invariant of the stress deviator). By applying a not too high compressive stress σ_{xx}, the hydrostatic pressure increases from p_a to $p = p_b = (\sigma_{xx} - \sigma_{yy})/3$, and the stress state corresponds to an expanded Mohr circle. Thus, p_b provides confinement, which increases the resistance τ from τ_a to τ_b, as shown in Fig. 7(*b*). Moreover, the numerical simulations show the active FPZ to become longer and narrower, which may be explained by a reduction of the average inclination of the microcracks from the macrocrack direction.

Regime 2: Expansive Slipping and Splitting: When, however, compression σ_{xx} is raised to approach the compressive stress limit, one must consider the Mohr circle shifted to the left in Fig. 7(*c*). The minimum principal stress indicates the uniaxial splitting strength of concrete, at which the FPZ is failing in compression due to σ_{xx}. The static friction on inclined microcracks in the FPZ is overcome and the cracks slip, which tends to widen the active FPZ and reduce the resistance to tensile stress σ_{yy} caused by bending, as intuitively explained by sliding over the entire FPZ portrayed in Fig. 7(*c*). This kind of failure mechanism has been observed in simulations with the crack-band microplane model, by inspecting the stresses and deformations in FPZ on microplanes of inclined orientations. Another possible mechanism is the growth and collapse of micropillars between splitting microcracks, between micropillar of width s [17], which also leads to lateral widening (Fig. 7(*b*)) and shortening of FPZ.

The widening and shortening of the FPZ in this regime is manifested in a decrease of c_f obtained from the size effect method. The widening of the FPZ is accompanied by widening of the crack or notch behind it, which further allows the compressed material at crack faces to expand into the crack space and thus reduces the resistance to compression. For zero crack-parallel compression, the gap test gave $G_f = 86.7$ N/m, which is within the range of values reported by many authors [14]. The characteristic length in this case is approximately 18 mm. This is about 1.5 times the average coarse aggregate size.

For a moderate crack-parallel compression, $\sigma_{xx} \approx 0.4\sigma_c$, the size effect analysis of the present test data yields $G_f = 154.2$ N/m, which roughly doubles the value at zero compression (Fig. 9(*a*)).

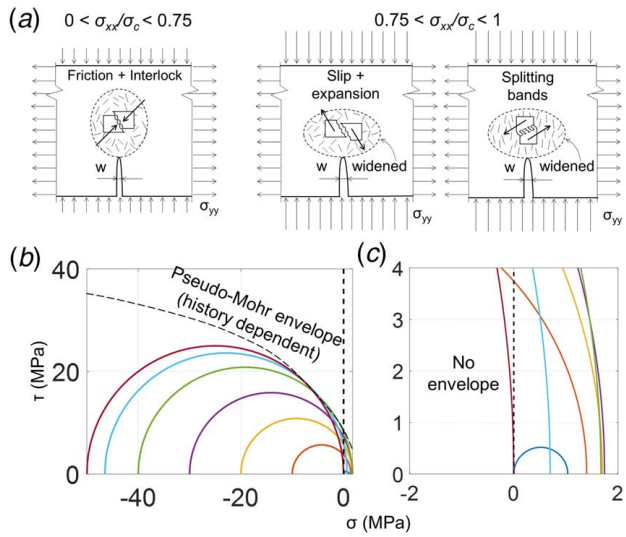

Fig. 7 (*a*) Suggested mechanisms for enhancement and diminishing of G_f; (*b*) Mohr circles corresponding to the M7-CBM predictions in Fig. 6(*a*)), with σ_{yy} = nominal strength at peak load for specimens of medium size; and (c) a closer look to the region of small σ_{xx}

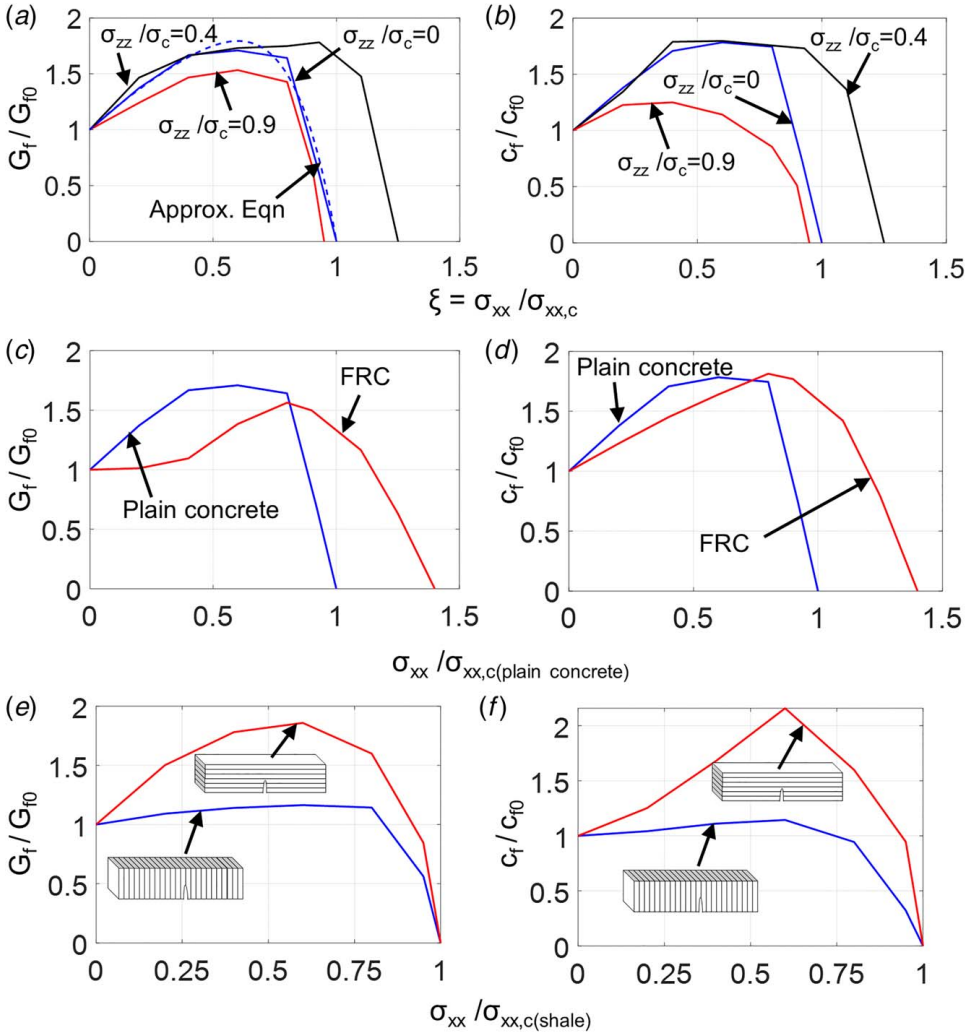

Fig. 8 (*a*) and (*b*) G_f and c_f as functions of σ_{xx} subject to different values of anti-plane stress σ_{zz} (with results approximated by Eq. (1)), (*c*)–(*d*) the variation of G_f and c_f of 3% Dramix-fiber-reinforced concrete as functions of σ_{xx}, and (*e*)–(*f*) the variation of G_f and c_f of shale with bedding plane normal and parallel to the crack as functions of σ_{xx}

The material characteristic length is also nearly doubled, to 37.1 mm, and the FPZ gets more elongated. Another consequence is that the postpeak softening slope gets less steep or that the snapback is suppressed.

For high crack-parallel compression at $\sigma_{xx} = 0.9\sigma_c$, the fracture energy is, by contrast, drastically reduced to $G_f = 51.2$ N/m (Fig. 7(*a*)). So is the value of characteristic length, 11.2 mm, which indicates a shorter and wider FPZ. As $D \to \infty$, the final asymptotic slope of LEFM, $-1/2$, is approached more quickly. Hence, the brittleness number D/D_0 [14,26] for a given D increases. After the experiments, the fractography showed small, crumbly pieces of nearly detached concrete, demonstrating the formation of small splitting microcracks and slip expansion. Another consequence is that the postpeak softening slope gets steeper or that snapback gets promoted.

5 Further Simulations of Crack-Parallel Stress Effect on G_f

5.1 Plane Strain and Anti-Plane Normal Strain Effects. Another interesting aspect is the effect of the anti-plane stress σ_{zz}. For σ_{zz} applied on the entire side faces of the present specimens of three sizes, several simulated curves of $G_f(\sigma_{xx})$ are plotted in Figs. 8(*a*) and 8(*b*) for various ratios σ_{zz}/σ_c. Obviously, in this case (apparently never studied before), σ_{zz}, too, has a significant effect.

5.2 Fiber-Reinforced Concrete. Short random fibers change significantly the postpeak softening damage in concrete. Microplane model M7f was calibrated to capture it [30] and has been used to simulate G_f for the present specimen geometry (see Figs. 8(*c*) and 8(*d*)). Due to the lack of material for calibration, we extrapolated the currently used model, using default material parameters, to account for the presence of fibers. First, the parameters for plain concrete were determined from calibration as described in Appendix C. Later, the parameters related to fibers were obtained from Ref. [30] as if 3% Dramix fiber were mixed in the same batch of concrete. Later, the same set of different specimen sizes was numerically tested, and the results were provided in Figs. 8(*c*) and 8(*d*). Note that, this procedure complies with the calibration of M7f for FRC.

The presence of fibers enhances the cohesive strength and the crack bridging effect, which gives a higher G_f at zero σ_{xx}. Therefore, a mild increase of σ_{xx} also shows a relative increase in G_f, but with a

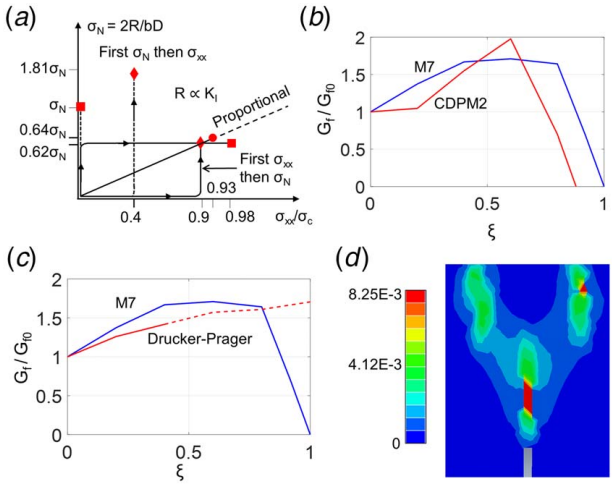

Fig. 9 (*a*) History dependence of the stress path, (*b*) G_f as a function of σ_{xx} predicted by tensorial models with invariants by Grassl et al. [43] σ_{xx}, (c) G_f as a function of σ_{xx} predicted by tensorial Drucker–Prager model [44], and (*d*) a premature failure predicted by D–P ahead of the main crack tip before moment *M* is applied

lower magnitude. This probably stems from the fact that the effect of fibers on the friction boundary is weaker than on the normal boundary of M7, i.e., the fibers are more effective in bridging the opening microcracks than in preventing their sliding. Furthermore, the decline in G_f toward zero is more gradual than in plain concrete. This phenomenon originates from the inhibition of splitting microcracks, so that a higher σ_{xx} is needed to cause slip expansion and the energy dissipation becomes more gradual (see Fig. 7).

5.3 Shale. The recently developed spherocylindrical microplane model for shale [31], intended for the simulation of hydraulic fracturing, can capture the effect of anisotropy due to bedding layers on the damage development in shale. The orientation of the crack plane relative to bedding layers matters. Because the overburden pressure is approximately the double of the horizontal tectonic stresses and the bedding layers are nearly horizontal, we simulated a shale specimen of the present geometry with a crack normal to the bedding layers. For comparison, we added the case of a crack parallel to the bedding layers. The parameters were obtained from a previous calibration on Longmaxi shale [31], and the resulting curves of G_f versus σ_{xx} is shown in Figs. 8(*e*) and 8(*f*). In the case of the crack normal to the bedding plane, the crack must cut through these layers which are stronger than the interlayer material. Thus, a higher energy release is required, which explains why compressive σ_{xx} leads to much higher relative G_f values than those for cracks parallel to bedding layers, as seen in Fig. 8(*e*).

5.4 History Dependence of the Crack-Parallel Stress. To demonstrate the path dependence, which is ignored by any formula for G_f (such as Eq. (1)), Fig. 9 presents, for the mid-size concrete specimen, the M7 simulations for four different paths (or histories) of $2R/bD$ versus σ_{xx}, where R is the beam end reaction that produces the bending moment, M, to which the stress-intensity factor K_I is proportional. (1) The first path is a simple increase of R at $\sigma_{xx} = 0$ up to failure, which defines the nominal strength σ_N. (2) In the gap test path, as already described, a high crack-parallel compression $\sigma_{xx} = 0.9\sigma_c$ is applied first, and the subsequent path segment with increasing R ends up with the failure value of $2R/bD = 0.62\sigma_N$, as seen in Fig. 6. (3) When, however, the end reaction, $R = 0.62\sigma_N$ is applied first (which would require a more complex test setup and controls), and the crack-parallel compression σ_{xx} is subsequently increased up to failure, the failure occurs at significantly higher compression σ_{xx} (because FPZ was less damaged during the first segment of the path). (4) When only a moderate crack-parallel compression $\sigma_{xx} \approx 0.4\sigma_c$ is applied first, the reaction R can be increased to a much higher value, with $2R/bD = 1.81\sigma_N$. (5) For proportional loading whose straight path passes through the terminal point of gap test, case (2), the G_f is 11% larger than in the gap test.

5.5 Comparisons With Tensorial Plastic-Failure Models. *Model CDPM2*—constitutive damage plastic model for concrete of the classical type, defined in terms of stress and strain tensors and their invariants. This is an excellent model that has recently been developed by Grassl et al. [43], within the framework of tensorial plasticity with damage. The G_f variation obtained with this model is shown in Fig. 9(*b*). The qualitative trend obtained reflects both the strengthening and weakening phases of G_f evolution, but the differences from M7 are significant, and the deviations from the gap test in the last weakening phase is large.

Drucker–Prager and Mohr–Coulomb model from ABAQUS: The G_f evolution calculated with the classical Drucker–Prager's (D–P) model [44] is presented in Fig. 9(*c*). The strengthening phase is represented, but there is no weakening phase. For this model, the uniaxial compression stress test produces bulging at mid-length of the specimen rather than formations of splitting cracks and inclined shear bands. The strengthening phase gets captured because the D–P describes well the frictional resistance to slip and interlock under under triaxial confinement. It should also be mentioned that, at high compression σ_{xx}, the size effect method is inapplicable because there exists a premature compression failure at the crack front. This gets manifested as a macro-crack in front of the notch, which significantly lowers the peak load, especially in the largest specimens (Fig. 9(*d*)). This stems from the fact that the largest specimens are less confined by the boundary. Therefore, at higher compression, the size effect G_f had to be computed from linear regression of the results for only the small-size and mid-size specimens, as represented by the dashed curve segment in Fig. 9(*c*).

Mohr–Coulomb concrete model with a cap, from ABAQUS: Unlike the D–P, the Mohr–Coulomb's model [45] produces an artificial stiffening effect at the crack tip, even at zero σ_{xx}. Therefore, it appears inapplicable for fracture analysis.

Does Mohr failure envelope exist? This question was briefly addressed in Ref. [1], in which it was shown that the Mohr circles for the states at P_{max} of concrete have no envelope. In Figs. 7(*c*) and 7(*d*), the same is now demonstrated for shale, using the results corresponding to the curve of G_f in Figs. 7(*c*) and 7(*d*).

5.6 Microplane Model Features Essential for Predicting G_f. The microplane model used in the present simulations is described in detail in Ref. [21]. Let us list here briefly the features of microplane model that are advantageous for the modeling of crack-parallel compression effects and distinguish it from the models based on tensors and their invariants.

(1) Whereas the microplane model calculates the strain tensor from the stress tensor, the constitutive equation is vectorial, calculating the stress vector from the strain vector on a generic plane of any orientation, called the microplane. The vectors, unlike tensors, can be semi-intuitively related to tensile crack opening, compression splitting or frictional slip.
(2) A big advantage is that one can capture the *vertex effect*, e.g., the fact that a shear stress increment applied after compressive stress in the inelastic range has incremental stiffness much smaller than elastic (even three-times lower, for concrete), while in all the classical tensorial models (Mohr–Coulomb, Drucker–Prager, von Mises, etc.), a stress increment parallel to the loading surface gives incorrectly, except at a vertex, an elastic incremental stiffness, even in damage states.

(3) Another advantage is that, in M7, the hydrostatic or uniaxial strain compression is always hardening, while the unaxial compressive stress gives a peak and postpeak softening.
(4) M7 also delivers correct hysteretic loops under cyclic loading and reproduces subcritical fatigue crack propagation up to several thousand cycles (in agreement with Paris law).

Early on it was thought that the microplane model was computationally too demanding. For one material point, it may run ten-times longer than a tensorial constitutive law. But for a system of millions of finite elements, tractable today, the difference in running time is imperceptible because the computational work increases, with the number of displacements, quadratically, but on the constitutive law only linearly.

6 Limitations of Cohesive Crack Model and LEFM and Contrast With Crack Band Model

The present results highlight the limitations of the cohesive crack model (CCM) for quasibrittle materials. In the case of Mode I fracture, this model is defined by a scalar relation between the crack-bridging, or cohesive, normal stress and the relative normal displacement across the crack. In the case of mixed mode fracture, the model is defined by a relation of crack-bridging normal and shear stresses to the relative normal and shear displacement. But the crack-parallel normal stresses (and strains) cannot be included as the basic force and displacement variables. They can be considered only as parameters affecting the material fracture properties. For the effect of σ_{xx}, Ref. [1] gives the formula

$$\frac{G_f}{G_{f0}} = 1 + \frac{a}{1 + b/\xi} - \frac{1 + a + b}{1 + b}\,\xi^s \tag{1}$$

where $\xi = \sigma_{xx}/\sigma_{xx,c}$ and $\sigma_{xx,c}$ at $\sigma_{pad} = \sigma_c$. The curve in Figs. 3(*a*) and 3(*b*) is well approximated by $a = 1.038$, $b = 0.245$, $s = 7.441$ (as shown by dashed curves). These values will, of course, be different for different materials, structure sizes, load histories, σ_{zz}/σ_{xx} ratios, etc.

A fully realistic model for quasibrittle fracture must, therefore, describe well the microscale mechanisms mentioned earlier. This can be a tensorial law, with the FPZ described by a tensorial damage constitutive model with strain softening, coupled with some form of a localization limiter or mesoscale discrete model. The simplest and most widely used model is the crack-band model coupled with a physically realistic form of the continuum damage model, here the microplane model, underlying the present simulations.

It should be noted in Fig. 6(*b*) that there exists a threshold at which the crack-parallel compressive stress σ_{xx} turns from strengthening to weakening of the fracture resistance. For the present concrete, it is $\sigma_{xx} \approx -0.75\sigma_c$. No doubt this threshold varies among different materials, and for some, the strengthening phase might not exist. This might be the case for some uniaxial laminate fiber composites, notoriously weak in compression.

From the microplane simulations, it is clear that the microcracking in the FPZ produced by high crack-parallel compressive stress σ_{xx} must increase permeability in the FPZ and in its wake, as the crack propagates. This is important for various geomechanics problems and particularly for hydraulic fracturing (or fracking) of gas or oil shale. In Ref. [46], it was shown that the permeability and reduced transverse Biot coefficient due to preexisting microcracks with its Biot coefficient are what causes the hydraulic cracks to branch sideways from the wall of a primary hydraulic crack. The present analysis shows that the propagations of the primary crack and secondary branched cracks must be strongly affected by the crack-parallel overburden and tectonic stresses, which are about 80 MPa and 40 MPa at the typical depth of fracking, about 3 km.

Because of their simplicity, scalar models for softening damage have become popular for crack band representation of fracture. Some examples are Mazars' isotropic damage model for concrete [47], the nonlocal damage model [48], and all other models using the Kachanov–Hult–Lemaitre type scalar damage measure ω. These damage laws may be unrealistic for two reasons—first, they have not been calibrated by various types of triaxial material tests on specimens of sizes nearly equal to the FPZ (or RVE) size (see 21 types of such tests used to calibrate M7 in Ref. [29]). Second, their use of a single scalar damage parameter, ω, varying between 0 and 1, appears too restrictive (the microplane model and fracture characteristics has several independent damage parameters). All these models are usable only if the crack-parallel normal stress is a priori known to be negligible (or below about 10% of compressive strength) in all the finite elements within the damage zone. As for peridynamics, no comments are necessary [49].

The fracture models characterized only by G_f can be used if reprogrammed to vary G_f as a function of the crack-parallel stresses, σ_{xx} and σ_{zz}. This, of course, ignores history effects, whose severity has not yet been clarified. As for the cohesive crack model, its softening stress-displacement law would have to be varied depending on σ_{xx} and σ_{zz}. But this brings up the questions of whether the cohesive softening curve should be scaled vertically or radially as a whole (which would scale both G_F and G_f), or only in its initial part (controlled by G_f only), what should be the proportion of such scalings, and whether a horizontal scaling is also necessary. Again, this would miss history effects.

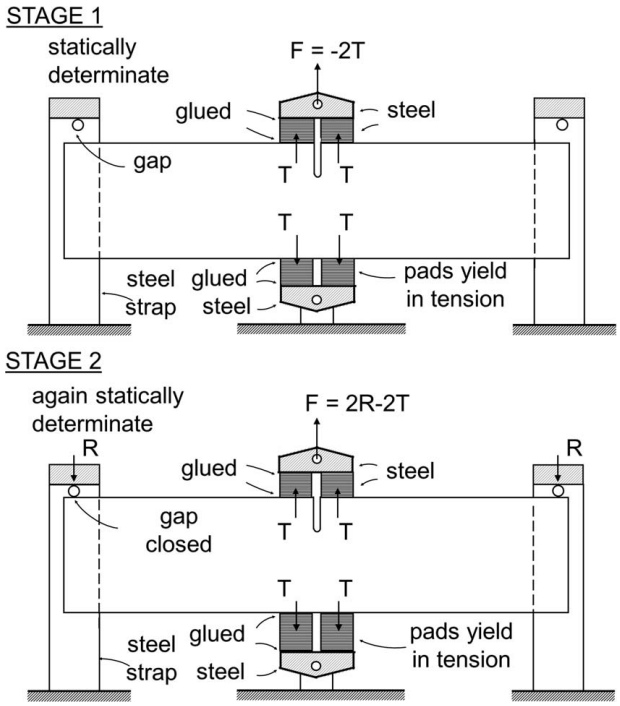

Fig. 10 Gap test for crack-parallel tension

7 Gap Test for Crack-Parallel Tension

Finally, it may be pointed out that the gap test may be easily adapted to measure the effect of crack-parallel tension on G_f. The setup shown in Fig. 10 is self-explanatory.

8 Conclusions

(1) Moderate crack-parallel compressive stress, in-plane or out-of-plane, drastically increases, even doubles, the Mode I fracture energy G_f (or fracture toughness K_{Ic}) of concrete, and probably also of shale and various rocks, coarse-grained ceramics and sea ice. This can be explained by an increase of hydrostatic pressure raising friction on inclined planes.

(2) High crack-parallel compressive stress, close to the compression strength limit, drastically decreases G_f and eventually reduces it to zero. This can be explained by frictional slip on inclined planes and splitting microcracks, causing lateral dilation.
(3) The cohesive crack model (CCM), as a line crack model with a scalar relation between crack-bridging stress and relative displacement of crack faces, cannot capture these phenomena, since the crack-parallel strains are not the thermodynamic variables in this model. Hence, σ_{xx} and σ_{zz} must be used as parameters which, however, appear to be only a crude approximation that cannot capture the effect of the triaxial stress and strain history. The same objection also applies to the recent cohesive crack model that is enriched with crack-parallel strain by shrinking a crack band into a line [50].
(4) To capture the experimentally evidenced effect of crack-parallel compression in general, either a microscale descriptive model or a tensorial constitutive model for softening damage must be used. This is effectively done with the crack-band model coupled with the microplane damage constitutive law. This law can mimic the effects of inelastic frictional slips and microcrack formation on planes of different orientations. The damage laws in the phase-field models restricted to only a single damage parameter do not appear to be realistic and require improvement.
(5) Linear elastic fracture mechanics cannot capture the effect of crack-parallel compression. CCM, as a line crack model, can neither. Nor can the computational models based on LEFM or CCM.
(6) An effective method for fracture testing with crack-parallel compression is the gap test, in which the compression is generated by plastic pads capable of perfectly plastic yielding, and the supports are installed with a gap that closes only after the pads begin yielding. The gap test is possible for both compressive and tensile crack-parallel stress.
(7) The results are of particular interest for (a) the shear failure of reinforced concrete beams and punching failure of slabs; (b) fracture of prestressed concrete, (c) hydraulic fracturing of shale, at which the overburden and tectonic stress introduce significant crack-parallel compression; (c) fiber composites, where buckling of embedded fibers reduces compression strength; (d) propagation of the front of slip on earthquake fault, subjected to enormous crack-parallel tectonic and overburden stresses; (e) splitting fracture of sea ice plates pushing against fixed objects, or in front of icebreaker; (f) burst of very deep boreholes and mine stopes; (g) high biaxial tensile stresses in composite aircraft fuselage; and (h) cyclic and static fatigue crack growth under crack-parallel in-plane and out-of-plane stresses, etc. Ofen the crack-parallel compression is so high that the effective Mode I fracture energy (or stress-intensity factor) is nearly zero.
(8) The Mohr circles for various levels of crack parallel stress in shale do not have an envelope. Therefore, the general use of Mohr–Coulomb failure criterion for shale or other quasibrittle materials is unwarranted.

Note: A powerful alternative to the present analysis of concrete is the lattice discrete particle model (LDPM) [51,52] mimicking the heterogeneous microstructure and mesoscale interactions. It will be pursued in a forthcoming paper (also it may be remarked that performing more than 27 experiments was prevented by the current virus pandemic).

Conflict of Interest

There are no conflicts of interest.

Data Availability Statement

The datasets generated and supporting the findings of this article are obtainable from the corresponding author upon reasonable request. The authors attest that all data for this study are included in the paper. Data provided by a third party are listed in Acknowledgments. No data, models, or code were generated or used for this paper.

Appendix A: Alternative Test Methods and Related Previous Studies

As an alternative to the present test, a system of two balance beams shown in Fig. 11 was fabricated and tried to provide reactions at both beam ends and notch corners. The ratio of these reactions was controlled by moving the locations of the supports at base. But it proved tricky to keep the system stable and properly aligned before applying the load. Another bigger problem was seen in the evaluation. This test would have to be conducted for several different specimen sizes D and, with heavy I-sections which must provide a large enough stiffness even for the largest specimen size. The self-weight of these I-sections would add up to σ_{xx} or bending moment non-proportionately, which will create complication for the fracture analysis. The biggest problem is that the compressive force would not be constant but (in theory) raised proportionally, which would make it difficult to deduce the effect of σ_{xx} on G_f. Since σ_{xx} does not matter for the size effect method, this method could still be used, but it would deliver a fracture energy corresponding to a certain history of σ_{xx} rather than to any specific value of G_f. Complex optimization of tests with many different histories, using an assumed constitutive damage law, would be required, to obtain the effect of σ_{xx} on G_f, inevitably quite ambiguous. The constancy of σ_{xx} is what makes the gap test simple and unambiguous.

Additional hydraulic jacks were used in 1995 in a pioneering study by Tschegg et al. [53], to introduce crack-parallel compression in an elaborate modification of the wedge-splitting test. The results confirmed the hint from the 1987 microplane model that crack-parallel compression should have some effect but no clear conclusion was could be drawn. However, the evaluation was aimed at G_F rather than G_f, and thus was compromised by the shape, unknown at that time, of the complete softening law with its long tail (as in Fig. 1). The evaluation also suffered from the complexity of stress field in which the maximum compression occured away from the notch tip, and also from the effects of bending moment due to the weight of clamping frames and hydraulic jacks, as well as from the friction under the jacks. The main

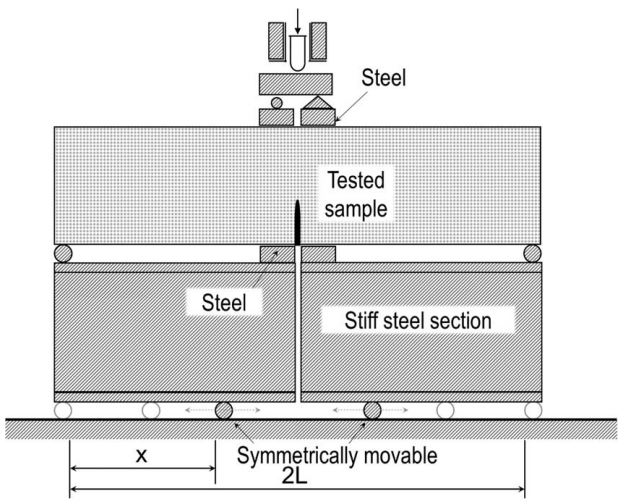

Fig. 11 An alternative test method considered to generate σ_{xx} with proportional loading

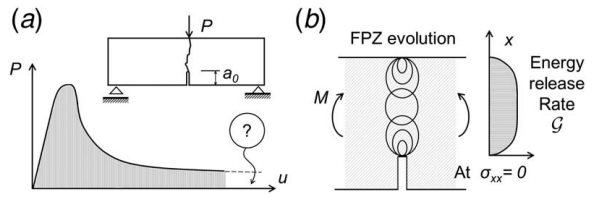

Fig. 12 Load deflection curve in work-of-fracture test: (*a*) with a long tail hard to capture completely and (*b*) growth of FPZ at the start of crack propagation from the notch, and decrease at the end

problem, unknown in the 1990s, was that the G_F evaluation by the work-of-fracture method gives rather ambiguous results unless scaled tests are performed for several sufficiently different sizes [25]. Another serious problem was that the energy dissipation rate (or the J-integral) is markedly reduced during the initial formation of the FPZ near the notch tip and during the terminal phase on approach to the opposite phase (Fig. 12).

If the FPZ is not small compared to the ligament cross section, which is always the case for concrete, the work-of-fracture per unit crack length severely underestimates the steady-state energy dissipation and causes a major error.

As another alternative, one might also think of imposing a compressive displacement with pair of stiff clamping frames mounted on the beam. But the stress induced would relax (by about 30%), due to concrete creep and shrinkage during the test. To get G_f as a function of strain ϵ_{xx} instead of σ_{xx}, the clamping frames would have to be very stiff and heavy, to maintain constant ϵ_{xx}, and would have different relative weights for different specimen sizes. Another possibility would be hydraulic flat jacks within these frames, similar to those of Tschegg but equipped with computer control. Interpretation would anyway be fraught with ambiguity.

For metals assumed to follow the Ramberg–Osgood J_2 power-law hardening plasticity, Refs. [54–57] showed analytically, in the early 1990s, that the in-plane crack-parallel stress (called the T-stress) and generally the stress triaxiality affect the J-integral and the singular plastic-hardening HRR field surrounding a sharp crack tip. But, as commented on in more detail in Ref. [1], these are different problems. The present analysis does not apply to metals (with the probable exception of the micrometer scale). Furthermore, Cotterell and Rice [58] showed analytically that a high T-stress may cause the LEFM crack path to deflect sideways, but this, too, is a different problem.

Appendix B: Concrete Characterization and Further Gap-Test Details

To minimize the scatter of mechanical properties, all the specimens were cast within a few hours from the same batch of concrete delivered by a ready-mix supplier (Ozinga Co.). Normal concrete of specific compression strength $f'_c = 27.58$ MPa (4000 psi) at 28 days of age was used. The slump range was 7.62–12.70 cm (3.00–5.00 in.), and the specific air content was within 0–3%. In the mix, one cubic yard contained 470 lb. of cement (ASTM C150, 100 lb. of blast-furnace slag (labeled C989), 1750 lb. of coarse aggregate (ASTM C33#67), 1500 lb. of fine aggregate (ASTM C33#2); water-cement ratio $w/c = 0.45$.

The specimens for material characterization and model calibration (Fig. 1) included cylinders for compression tests of diameter 101.6 mm and length 203.2 mm; square prisms for compression tests of side 76.2 mm and length 152.4 mm; cylinders for splitting tests of diameter 101.6 mm and length 203.2 mm; and prisms for splitting tests of side 76.2 and length 152.4 mm. The beams for fracture tests, geometrically scaled, were of three sizes: small: 101.6 × 101.6 × 406.4 mm, medium: 101.6 × 203.2 × 812.8 mm, and large: 101.6 × 203.2 × 812.8 mm. The notch/depth and span/depth ratios were $a/D = 0.3$ and $2L/D = 3.75$, respectively. The elasto-plastic loading pads had sides S of ratio $S/D = 1/4$ (Fig. 1(*e*)). All the specimens were tested within 3 weeks, but the effect of this age difference on the degree of hydration and strength was negligible since the specimens were 1-year old. The specimens were all cured in a fog room until the time of test.

Appendix C: Material Calibration Experiments

Aside from the results of the gap tests for different specimen sizes at zero σ_{xx}, the properties of concrete were calibrated by tests of uniaxial compression of cylinders and prisms (Fig. 13(*a*)). These calibrations are sufficient for M7 to characterize the behavior of normal concrete, which was validated by Brazilian splitting tests on both cylinders and prisms (see Fig. 13(*b*), where the error bars indicate one standard deviation based on four tests for each case. The same model was utilized to predict the results of the gap test at non-zero σ_{xx}. For uniaxial compression, the specimens were capped with sulfur to make sure the loaded surface would be flat and almost frictionless. Linear variable differential transformers (or LVDT) were used to record two crack-parallel displacements, as well as one lateral displacements used to control the loading (see Figs. 1(*a*) and 1(*b*) (ASTM C39)). In the Brazilian tests (Figs. 1(*c*) and 1(*d*)), the loading strip was 12.7 mm wide and the samples were held in place at the beginning by a mild pressure (ASTM C496). The uniaxial tests of specimens of both types were conducted in the Tinus Alson frame with maximum load of 1000 kips, and the Brazilian splitting tests were done in the MTS loading frame of capacity 50 kips, both at the loading rate of 0.00635 mm/s. Every test took approximately 0.5 h.

Figure 13 shows the results for the uniaxial compression strength of cylindrical and prismatic specimens (Figs. 3(*a*) and 3(*b*)) and their corresponding Brazilian splitting tensile strengths (Fig. 3(*c*)). In Figs. 3(*a*) and 3(*b*), the dashed curve shows the upper and lower envelope of the data from three tests, whose average is represented by the dotted curve. This result is consistent with the average strength $f'_c = 42.74$ MPa reported by concrete supplier. Optimum fits of these results were obtained with the microplane constitutive

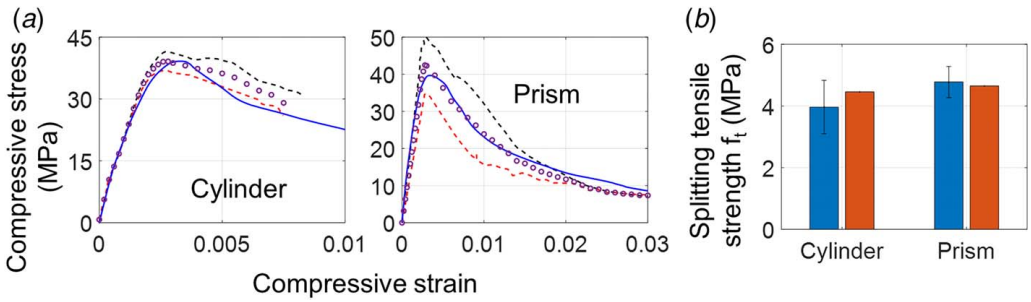

Fig. 13 Calibrations and validations to obtain parameters for M7-CBM: (*a*) uniaxial compression of cylinders and square prisms and (*b*) Brazilian splitting tests

model M7 [21,29] shown by solid curves. The M7 was implemented in ABAQUS using the crack-band model with element size 12 mm. The dotted and solid curves are consistent and serve to indicate the level of compression on notched beams.

Appendix D: Compression Stiffness of Plastic Pads and Their Optimization

For simplicity, consider a circular pad with radius r and polymer layer thickness h (Fig. 13). In the plastic regime, we assume the polymer is incompressible and has a very small but non-zero shear modulus μ (if μ were zero, the plasticized polymer would flow out). The boundaries of the layer are confined and behave as rigid. Volume conservation in the disc of radius $x \le r$ requires that $\pi x^2 w = 2\pi x h \bar{u}$, where w is the relative displacement of decrease of thickness and $\bar{u}$ is the average increase of radius x. Hence, $\bar{u}=wx/2h$. Given that the polymer does not slide on the layer surfaces, we may assume the radial displacement profile across layer thickness to be parabolic (Fig. 12). In that case, the maximum displacement is 1.5× higher than $\bar{u}$, the mean, and thus, the profile of shear angle is $\gamma = \partial u/\partial y = 6wxy/h^3$, where y is the transverse coordinate. The strain energy density with respect to radial coordinate x then is $\bar{W}(x) = 2\int_0^{h/2} \mu\gamma^2/2\mathrm{d}y = 3\mu w^2 x^2/2h^3$. Conservation of energy requires the work of compression of the layer by w to equal the strain energy increment of the whole layer, i.e., $W = Hw^2/2 = \int_0^r \bar{W}\cdot 2\pi x\,\mathrm{d}x$ where H is the compression stiffness of the layer. Integration yields

$$H = k_p \mu A^2/h^3, \quad k_p = 3/2\pi \tag{D1}$$

where $A = \pi r^2$ is the area of the pad. This equation may also be used as an approximation for a square pad of the same area (an accurate solution is more complicated). The pads should be shaped so as to minimize H (subject to Haringx's critical load formula [59] for shear buckling governing the elastomeric bearings of bridges), or minimizing A, which means replacing one pad with several small ones (or drilling big holes). Harigngx's formula gives the critical ratio $\lambda_{cr} = \sqrt{A}/h$ for buckling.

Second, let us analyze an elongated $l \times L$ rectangle (the pad in Fig. 14), with $L \gg l$, approximately in 1D, coordinate x. Due to incompressibility, the axial strains are distributed as $\bar{u} = (w/h)x$ and the strains are $\gamma = (12\bar{u}/h^3)y$. The work per unit length in x is $\bar{W} = 2\int_0^{h/2} \mu\gamma^2/2\mathrm{d}y = 6\mu w^2 x^2/h^3$. By integration, $W = 2b\int_0^{l/2} \bar{W}\mathrm{d}x = b\mu w^2 l^3/2h^3$. Setting $W = \frac{1}{2}Hw^2$, we get

$$H/b = \mu(l/h)^3 \tag{D2}$$

The same formula approximately applies to an annular pad with internal and external radii r_1 and r_2 provided that $l = r_2 - r_1 < r_1/4$. It also roughly applies to a pad with many sufficiently big regularly spaced holes (Fig. 14) of radius r provided that approximately $\sqrt{A/A_s - 1} < 1/4$ where A is the total area and A_s is the area of the holes. If >1/4, one can interpolate. Other polymers, e.g., high-density polyethylene, HDPE, can be also used to get a different μ. A possible alternative to the plastic pads are blocks of perfectly plastic metal, e.g., tin (Sn).

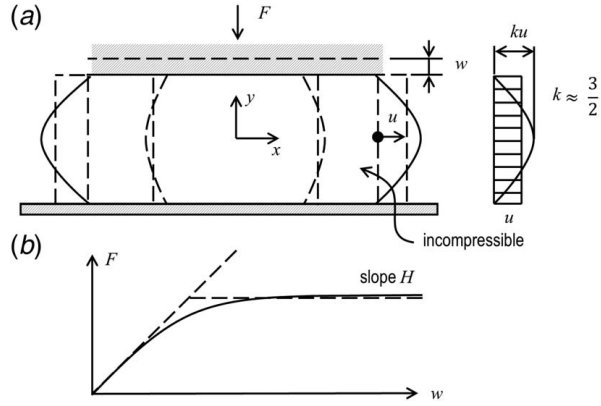

Fig. 14 (*a*) A circular plastic pad under compressive force and (*b*) the shape of the pad should be designed to minimize *H*

Appendix E: Size Effect Method to Identify G_f and c_f

To determine G_f, one needs the LEFM stress-intensity factor, K_I [14,26]. Although the load configuration is close to three-point bending, four-point-bending with a small but finite distance between the loads gives better accuracy (Fig. 3(*c*)). According to Ref. [60],

$$K_I = \sigma_N \sqrt{D} k(\alpha), \quad \text{where } \sigma_N = P/bD(\alpha = a/D) \tag{E1}$$

$$k(\alpha) = \frac{1.1682(2l-s)\sqrt{\pi\alpha}}{8\beta^{3/2}}(5 - 10\alpha/3 + \alpha^2 + 40\alpha^2(1-\alpha)^6 + 3e^{-6.134\alpha/(1-\alpha)}) \tag{E2}$$

where P is the total load (sum of two loads) applied at center span, σ_N is the nominal strength of beam, $2L$ is the span between the supports, S is the distance between the two center-span loads; $l = L/D$, $s = S/D$; b, D is the thickness and depth of beam; a is the crack (or notch) length, $\alpha = a/D$ is the relative crack length; σ_N is the nominal bending strength for each size; and $f(\alpha)$ is the dimensionless stress-intensity factor. The size effect law (SEL) reads:

$$\sigma_N = Bf_t(1 + D/D_0)^{-1/2} \tag{E3}$$

$$1/\sigma_N^2 = (1/B^2 f_t^2 + D/B^2 f_t^2 D_0) \;\Rightarrow\; Y = C + AD \tag{E4}$$

For data fitting, the SEL may be converted to a linear regression plot of $1/\sigma_N^2$ versus D as in Eq. (E4) [14,61]. To determine the size effect parameters, we need not only $k(\alpha)$ but also its derivative [14,26]:

$$\begin{aligned} k'(\alpha) = \frac{\mathrm{d}k(\alpha)}{\mathrm{d}\alpha} = {} & \frac{0.8411(2l-s)\sqrt{\pi}}{8(1-\alpha)^{3/2}\sqrt{\alpha}}\left(5 - 10\alpha/3 + \alpha^2 + 40\alpha^2(1-\alpha)^6 + 3\,e^{-6.134\alpha/(1-\alpha)}\right) \\ & + \frac{2.523(2l-s)\sqrt{\pi\alpha}}{8(1-\alpha)^{5/2}}\left(5 - 10\alpha/3 + \alpha^2 + 40\alpha^2\beta^6 + 3\,e^{-6.1342\alpha/(1-\alpha)}\right) \\ & + \frac{1.6823(2l-s)\sqrt{\pi\alpha}}{12(1-\alpha)^{3/2}}(-5 + 3\alpha + 120\alpha((1-\alpha)^6 - 360\alpha^2(1-\alpha)^5 \\ & - 27.6(1/(1-\alpha) + \alpha/(1-\alpha)^2)\,e^{-6.134\alpha/\beta}) \end{aligned} \tag{E5}$$

Upon rearranging Eq. (E3) as linear regression and fitting maximum load data, Eq. (E4), the fracture energy and the characteristic material length (roughly 40% of actual FPZ length) can then be computed from Refs. [14,26]:

$$G_f = K_f^2/E, \quad K_f = Bf_t\sqrt{D_0}k(\alpha_0) \tag{E6}$$

$$c_f = \frac{D_0 k(\alpha_0)}{2k'(\alpha_0)} \tag{E7}$$

Note that the crack-parallel compression is not a parameter in LEFM, and so, in LEFM, it cannot affect function $k(\alpha)$ and the equations relating G_f and c_f to $k(\alpha)$.

References

[1] Nguyen, H., Pathirage, M., Rezaei, M., Issa, M., Cusatis, G., and Bažant, Z. P., 2020, "New Perspective of Fracture Mechanics Inspired by Novel Test With Crack-Parallel Compression," Proceedings of the National Academy of Sciences, in press.

[2] Griffith, A., 1921, "The Phenomena of Rupture and Flow in Solid, Philosophical Translation," Royal Society of London, Series A, Vol. 221.

[3] Barenblatt, G., 1959, "Equilibrium Cracks Formed on a Brittle Fracture," Dokl. Ak. N., **127**, pp. 47–50.

[4] Barenblatt, G., 1962, "The Mathematical Theory of Equilibrium Cracks in Brittle Fracture," Adv. Appl. Mech., **7**(1), pp. 55–129.

[5] Cusatis, G., Bažant, Z., and Cedolin, L., 2003, "Confinement-Shear Lattice Model for Concrete Damage in Tension and Compression: II. Computation and Validation," J. Eng. Mech. – ASCE, **129**(12), pp. 1449–1458.

[6] Nemat-Nasser, S., and Horii, H., 1982, "Compression-Induced Nonplanar Crack Extension With Application to Splitting, Exfoliation, and Rockburst," J. Geophys. Res.: Solid Earth, **87**(B8), pp. 6805–6821.

[7] Madenci, E., 1991, "Slightly Open, Penny-Shaped Crack in An Infinite Solid Under Biaxial Compression," Theor. Appl. Frac. Mech., **16**(3), pp. 215–222.

[8] Lehner, F., and Kachanov, M., 2001, *On Modelling of "Winged" Cracks Forming Under Compression*, Springer, Dordrecht, Netherlands, pp. 73–75.

[9] Sahouryeh, E., Dyskin, A., and Germanovich, L., 2002, "Crack Growth Under Biaxial Compression," Eng. Fract. Mech., **69**(18), pp. 2187–2198.

[10] Wong, R., Tang, C., Chau, K., and Lin, P., 2002, "Splitting Failure in Brittle Rocks Containing Pre-Existing Flaws Under Uniaxial Compression," Eng. Fract. Mech., **69**(17), pp. 1853–1871.

[11] Zhou, X. P., and Wang, J. H., 2005, "Study on the Coalescence Mechanism of Splitting Failure of Crack-Weakened Rock Subjected to Compressive Loads," Mech. Res. Commun., **32**(2), pp. 161–171.

[12] Golshani, A., Okui, Y., Oda, M., and Takemura, T., 2006, "A Micromechanical Model for Brittle Failure of Rock and Its Relation to Crack Growth Observed in Triaxial Compression Tests of Granite," Mech. Mater., **38**(4), pp. 287–303.

[13] Yang, S., Dai, Y., Han, L., and Jin, Z., 2009, "Experimental Study on Mechanical Behavior of Brittle Marble Samples Containing Different Flaws Under Uniaxial Compression," Eng. Fract. Mech., **76**(12), pp. 1833–1845.

[14] Bažant, Z. P., and Planas, J., 1998, *Fracture and Size Effect in Concrete and Other Quasibrittle Materials*, CRC Press, Boca Raton, FL.

[15] Bažant, Z. P., and Oh, B. H., 1983, "Crack Band Theory for Fracture of Concrete," Matériaux et construction, **16**(3), pp. 155–177.

[16] Bažant, Z. P., Cervenka, J., and Wierer, M., 2001, "Equivalent Localization Element for Crack Band Model and As Alternative to Elements With Embedded Discontinuities," Fourth International Conference on Fracture Mechanics of Concrete and Concrete Structures, Cachan, France, May 28–June 1, Pergamon, Oxford, UK.

[17] Bažant, Z. P., and Xiang, Y., 1997, "Size Effect in Compression Fracture: Splitting Crack Band Propagation," J. Eng. Mech., **123**(2), pp. 162–172.

[18] Christoffersen, J., and Hutchinson, J., 1979, "A Class of Phenomenological Corner Theories of Plasticity," J. Mech. Phys. Solids, **27**(5), pp. 465–487.

[19] Bažant, Z. P., 1978, "Endochronic Inelasticity and Incremental Plasticity," Int. J. Solids Struct., **14**(9), pp. 691–714.

[20] Brocca, M., and Bažant, Z. P., 2000, "Microplane Constitutive Model and Metal Plasticity," ASME Appl. Mech. Rev., **53**(10), pp. 265–281.

[21] Caner, F. C., and Bažant, Z. P., 2013, "Microplane Model M7 for Plain Concrete. I: Formulation," J. Eng. Mech., **139**(12), pp. 1714–1723.

[22] Bažant, Z. P., and Pfeiffer, P. A., 1987, "Determination of Fracture Energy From Size Effect and Brittleness Number," ACI Mater. J., **84**(6), pp. 463–480.

[23] Cusatis, G., and Schauffert, E. A., 2009, "Cohesive Crack Analysis of Size Effect," Eng. Fract. Mech, **76**(14), pp. 2163–2173.

[24] Bažant, Z. P., and Yu, Q., 2011, "Size-Effect Testing of Cohesive Fracture Parameters and Nonuniqueness of Work-of-Fracture Method," J. Eng. Mech., **137**(8), pp. 580–588.

[25] Hoover, C. G., and Bažant, Z. P., 2014, "Cohesive Crack, Size Effect, Crack Band and Work-of-Fracture Models Compared to Comprehensive Concrete Fracture Tests," Int. J. Fract., **187**(1), pp. 133–143.

[26] Bažant, Z. P., and Kazemi, M. T., 1990, "Size Effect in Fracture of Ceramics and its Use to Determine Fracture Energy and Effective Process Zone Length," J. Am. Ceram. Soc., **73**(7), pp. 1841–1853.

[27] Shah, S. P., 1990, "Size-Effect Method for Determining Fracture Energy and Process Zone Size of Concrete," Mater. Struct., **23**(6), p. 461.

[28] Cedolin, L., and Cusatis, G., 2008, "Identification of Concrete Fracture Parameters Through Size Effect Experiments," Cem. Concr. Compos., **30**(9), pp. 788–797.

[29] Caner, F. C., and Bažant, Z. P., 2013, "Microplane Model M7 for Plain Concrete. II: Calibration and Verification," J. Eng. Mech., **139**(12), pp. 1724–1735.

[30] Caner, F. C., Bažant, Z. P., and Wendner, R., 2013, "Microplane Model M7f for Fiber Reinforced Concrete," Eng. Fract. Mech., **105**, pp. 41–57.

[31] Li, C., Caner, F. C., Chau, V. T., and Bažant, Z. P., 2017, "Spherocylindrical Microplane Constitutive Model for Shale and Other Anisotropic Rocks," J. Mech. Phys. Solids, **103**, pp. 155–178.

[32] Bažant, Z. P., 1984, "Size Effect in Blunt Fracture: Concrete, Rock, Metal," J. Eng. Mech., **110**(4), pp. 518–535.

[33] Bažant, Z., 1997, "Scaling of Quasibrittle Fracture: Asymptotic Analysis," Int. J. Fract., **83**(1), pp. 19.

[34] Bažant, Z. P., 2002, *Scaling of Structural Strength*, CRC Press, Boca Raton, FL.

[35] Bazant, Z. P., and Le, J.-L., 2017, *Probabilistic Mechanics of Quasibrittle Structures: Strength, Lifetime, and Size Effect*, Cambridge University Press, Cambridge, UK.

[36] ACI Committee 446, 1992, Fracture Mechanics of Concrete: Concepts, Models and Determination of Material Properties 91.

[37] Shanley, F. R., 1947, "Inelastic Column Theory," J. Aeronaut. Sci., **14**(5), pp. 261–268.

[38] Bažant, Z. P., and Cedolin, L., 1993, "Why Direct Tension Test Specimens Break Flexing to the Side," J. Struct. Eng., **119**(4), pp. 1101–1113.

[39] Bažant, Z. P., and Cedolin, L., 2010, *Stability of Structures: Elastic, Inelastic, Fracture and Damage Theories*, World Scientific, Singapore.

[40] Nakayama, J., 1965, "Direct Measurement of Fracture Energies of Brittle Heterogeneous Materials," J. Am. Ceram. Soc., **48**(11), pp. 583–587.

[41] Tattersall, H. G., and Tappin, G., 1966, "The Work of Fracture and Its Measurement in Metals, Ceramics and Other Materials," J. Mater. Sci., **1**(3), pp. 296–301.

[42] Hillerborg, A., Modéer, M., and Petersson, P.-E., 1976, "Analysis of Crack Formation and Crack Growth in Concrete by Means of Fracture Mechanics and Finite Elements," Cem. Concr. Res., **6**(6), pp. 773–781.

[43] Grassl, P., Xenos, D., Nyström, U., Rempling, R., and Gylltoft, K., 2013, "Cdpm2: A Damage-Plasticity Approach to Modelling the Failure of Concrete," Int. J. Solids Struct., **50**(24), pp. 3805–3816.

[44] Drucker, D. C., and Prager, W., 1952, "Soil Mechanics and Plastic Analysis or Limit Design," Q. Appl. Math., **10**(2), pp. 157–165.

[45] Nadai, A., 1950, *Theory of Flow and Fracture of Solids, V1*, McGraw-Hill, New York, NY.

[46] Rahimi-Aghdam, S., Chau, V.-T., Lee, H., Nguyen, H., Li, W., Karra, S., Rougier, E., Viswanathan, H., Srinivasan, G., and Bažant, Z. P., 2019, "Branching of Hydraulic Cracks Enabling Permeability of Gas or Oil Shale With Closed Natural Fractures," Proc. Natl. Acad. Sci. U. S. A., **116**(5), pp. 1532–1537.

[47] Mazars, J., 1986, "A Model of a Unilateral Elastic Damageable Material and its Application to Concrete," Fract. Toughness Fract. Energy Concr., pp. 61–71.

[48] Pijaudier-Cabot, G., and Bažant, Z. P., 1987, "Nonlocal Damage Theory," J. Eng. Mech., **113**(10), pp. 1512–1533.

[49] Bažant, Z. P., Luo, W., Chau, V. T., and Bessa, M. A., 2016, "Wave Dispersion and Basic Concepts of Peridynamics Compared to Classical Nonlocal Damage Models," ASME J. Appl. Mech., **83**(11), p. 111004.

[50] Remmers, J. J., De Borst, R., Verhoosel, C. V., and Needleman, A., 2013, "The Cohesive Band Model: A Cohesive Surface Formulation With Stress Triaxiality," Int. J. Fract., **181**(2), pp. 177–188.

[51] Cusatis, G., Pelessone, D., and Mencarelli, A., 2011, "Lattice Discrete Particle Model (LDPM) for Failure Behavior of Concrete. I: Theory," Cem. Concr. Compos., **33**(9), pp. 881–890.

[52] Cusatis, G., Mencarelli, A., Pelessone, D., and Baylot, J., 2011, "Lattice Discrete Particle Model (LDPM) for Failure Behavior of Concrete. II: Calibration and Validation," Cem. Concr. Compos., **33**(9), pp. 891–905.

[53] Tschegg, E., Elser, M., and Stanzl-Tschegg, S., 1995, "Biaxial Fracture Tests on Concrete-Development and Experience," Cem. Concr. Compos., **17**(1), pp. 57–75.

[54] O'Dowd, N., and Shih, C., 1991, "Family of Crack-Tip Fields Characterized by a Triaxiality Parameter I. Structure of Fields," J. Mech. Phys. Solids, **39**(8), pp. 989–1015.

[55] O'Dowd, N., and Shih, C., 1992, "Family of Crack-Tip Fields Characterized by a Triaxiality Parameter II. Fracture Applications," J. Mech. Phys. Solids, **40**(5), pp. 939–963.

[56] Betegón, C., and Hancock, J., 1991, "Two-Parameter Characterization of Elastic-Plastic Crack-Tip Fields," ASME J. Appl. Mech., **58**(1), pp. 104–110.

[57] Tvergaard, V., and Hutchinson, J. W., 1992, "The Relation Between Crack Growth Resistance and Fracture Process Parameters in Elastic-Plastic Solids," J. Mech. Phys. Solids, **40**(6), pp. 1377–1397.

[58] Cotterell, B., and Rice, J., 1980, "Slightly Curved or Kinked Cracks," Int. J. Fract., **16**(2), pp. 155–169.

[59] Bažant, Z. P., and Beghini, A., 2006, "Stability and Finite Strain of Homogenized Structures Soft in Shear: Sandwich or Fiber Composites, and Layered Bodies," Int. J. Solids Struct., **43**(6), pp. 1571–1593.

[60] Fett, T., 2008, *Stress Intensity Factors — T-Stresses—Weight Functions*, KIT Scientific Publishing, Karlsruhe, Germany.

[61] Bažant, Z., Gettu, R., and Kazemi, M., 1991, "Identification of Nonlinear Fracture Properties From Size Effect Tests and Structural Analysis Based on Geometry-Dependent R-Curves," International Journal of Rock Mechanics and Mining Sciences & Geomechanics Abstracts, Vol. 28, Elsevier, pp. 43–51.